ADVANCED ENERGY MATERIALS
www.advenergymat.de

Optimization of Adsorption Sites for Selective Hydrobenzoin and Syngas Production in a Single Photoredox Cycle

Jian Lei, Hongyuan Yang, Bo Weng, Yu-Ming Zheng, Shifu Chen, Prashanth W. Menezes,* and Sugang Meng**

Integrating benzyl alcohol oxidation with carbon dioxide (CO_2) reduction in a single photoredox catalysis is of high economic and practical interest. However, it remains challenging to controllably regulate the selectivity of specific C—C coupling chemicals (oxidation products) and the ratio of carbon monoxide and hydrogen (CO/H_2) for syngas (reduction products). Herein, an efficient photocatalyst consisting of CdS nanorods decorated by Ni_2P (NP/CdS) is developed, which achieves remarkable performance, producing C—C coupling hydrobenzoin (HB) with an excellent yield of ≈315.4 µmol g^{-1} h^{-1} and selectivity of ≈90%. This performance originates from the optimized adsorption of benzaldehydes and protons, promoting the generation of the critical radical intermediates (•CH(OH)Ph). Meanwhile, the favorable desorption of •CH(OH)Ph and HB from the binding sites is attained. On the other hand, by increasing the Ni_2P content in NP/CdS, the CO/H_2 ratio can be adjusted across a wide range (from ≈15:1 to ≈2.6:1), enabling syngas compositions suitable for industrial feedstock applications. This tunability is attributed to the lower CO_2 affinity of the Ni_2P phase compared to CdS while demonstrating higher activity for H_2 evolution. This work presents a novel approach for selectively and efficiently producing HB and tunable syngas simultaneously.

1. Introduction

The selective transformation of aromatic alcohols into high-value C—C coupling products is crucial for industrial applications and laboratory research.[1–4] Traditional methods often involve the use of toxic cyanides and metal complex catalysts, resulting in the production of various byproducts.[5–7] Within this context, photocatalytically facilitating the dehydrogenative coupling of aromatic alcohol into C—C coupling compounds, particularly utilizing green energy input like visible-light irradiation, offers a sustainable and promising alternative.[8,9] However, due to the relative reactivity of the hydroxyl group in alcohols, the cleavage of C—O and/or O—H bonds is inherently easier than C—H bonds in aromatic alcohols,[10] making it difficult for direct photocatalytic conversion to coupling products. To address this

J. Lei, S. Meng
Key Laboratory of Green and Precise Synthetic Chemistry and Applications
Ministry of Education
College of Chemistry and Materials Science
Huaibei Normal University
Huaibei 235000, P. R. China
E-mail: sgmeng@chnu.edu.cn

B. Weng, Y.-M. Zheng
State Key Laboratory of Advanced Environmental Technology
Institute of Urban Environment Chinese Academy of Sciences
1799 Jimei Road, Xiamen 361021, P. R. China
E-mail: bweng@iue.ac.cn

The ORCID identification number(s) for the author(s) of this article can be found under https://doi.org/10.1002/aenm.202500950

DOI: 10.1002/aenm.202500950

B. Weng, Y.-M. Zheng
University of Chinese Academy of Sciences
19A Yuquan Road, Beijing 100049, P. R. China

H. Yang, P. W. Menezes
Department of Materials Chemistry for Catalysis
Helmholtz-Zentrum Berlin für Materialien und Energie
Albert-Einstein-Str. 15, 12489 Berlin, Germany
E-mail: prashanth.menezes@helmholtz-berlin.de, prashanth.menezes@mailbox.tu-berlin.de

P. W. Menezes
Department of Chemistry: Metalorganics and Inorganic Materials
Technical University of Berlin
Straße des 17 Juni 135. Sekr. C2, 10623 Berlin, Germany

S. Chen, S. Meng
Anhui Provincial Key Laboratory of Synthetic Chemistry and Applications
Huaibei Normal University
Huaibei 235000, P. R. China

challenge, facilitating the formation of critical carbon radical intermediates is essential for promoting C—C coupling, which can effectively boost the photocatalytic activity of the aromatic alcohol transformation. At the same time, in order to ensure selectivity, it is necessary to enable such radical intermediates to undergo C—C coupling with the adjacent intermediates instead of consecutive oxidation into the byproducts.[8,9,10]

Hydrobenzoin (HB) is a highly valuable commodity chemical, serving as a critical feedstock for the synthesis of additives and dyestuffs.[11] Recently, HB production through selective photocatalytic C—C coupling of benzyl alcohol (BA) has gained numerous research interest. Especially, the previous works demonstrated efficient and selective photocatalytic conversion of BA to HB, facilitated by the formation of carbon-centered •CH(OH)Ph radicals through the Cα–H cleavage of BA, which subsequently coupled with the adjacent •CH(OH)Ph.[12,13] However, if the as-obtained HB fails to desorb quickly from the catalyst surface, it risks further oxidation to benzoin or transformation into deoxybenzoin through a redox reaction.[9,13] As a result, it still remains a formidable challenge to selectively yield HB without the formation of other detectable C—C coupling byproducts through photocatalytic BA oxidation.

On the other hand, by fully utilizing the photogenerated charge carriers (holes and electrons), an efficient single photoredox catalysis system can selectively promote simultaneous oxidation and reduction reactions, enabling the production of valuable chemicals and fuels that are highly sought after by the industry and society.[14–16] In this regard, it is desirable to integrate aromatic alcohol oxidation with carbon dioxide (CO_2) reduction in a photoredox cycle, as it can not only yield value-added oxidative products (such as the abovementioned C—C coupling product HB), but also various useful reduction products. Among them, syngas, a mixture of CO and H_2, is particularly appealing due to its significance as an industrially important feedstock.[11,17] Notably, tuning the ratios of CO/H_2 in syngas broadens its application scope for various purposes.[11] To this end, incorporating different catalytic sites with inconsistent CO_2 affinities into a single catalyst during photoreduction has been proven to be an effective approach to altering the selectivity of CO and H_2, thus producing syngas with tunable CO and H_2 contents.[18,19] With these considerations in mind, an ideal photoredox cycle that integrates BA oxidation and CO_2 reduction would involve a targeted catalyst with active sites designed to simultaneously promote the formation and desorption of the •CH(OH)Ph radical intermediates and HB products while exhibiting different binding strengths to CO_2 reactants. This dual functionality could support the concurrent, highly selective, and efficient production of HB and syngas. Nevertheless, few studies to date have successfully accomplished this integration.

Herein, we present Ni_2P decorated CdS nanorods (NP/CdS) as a unique photoredox catalyst capable of simultaneously converting BA into HB with high yield and selectivity while reducing CO_2 into syngas with a tunable CO/H_2 ratio. The NP/CdS with optimal Ni_2P (12NP/CdS) can produce an impressive HB yield of ≈315.4 μmol g^{-1} h^{-1} with a high selectivity (≈90%). Meanwhile, syngas' CO/H_2 ratio can be fine-tuned from ≈15:1 to ≈2.6:1 by modulating Ni_2P content in the NP/CdS composite. The combination of comprehensive ex situ/in situ characterization and density functional theory (DFT) calculations reveal that the high HB activity and selectivity from BA transformation arises by the introduction of Ni_2P, which enable the active sites to more strongly adsorb benzaldehydes and protons, thereby promotion of the generation of •CH(OH)Ph intermediates and the subsequent C—C coupling into HB products. Remarkably, the facile desorption of •CH(OH)Ph and HB from the catalyst surface prevents the formation of undesired byproducts. On the other hand, the Ni_2P phase was verified to exhibit an inferior CO_2 affinity compared with CdS, but displaying a better H^* intermediate adsorption–desorption ability. By varying Ni_2P content, the active sites responsible for CO and H_2 generation can be regulated, and the ratio of these two reduction products can also be altered, resulting in a tunable syngas composition. Our work introduces a novel photocatalyst that selectively and efficiently generates C—C coupled HB and tunable syngas in a single redox cycle. This approach represents a new paradigm for effectively decreasing carbon emissions, solar energy conversion, and valuable chemical and fuel production.

2. Results and Discussion

2.1. Synthesis and Structural Characterizations

A series of CdS nanorods decorated by varying mass fractions of Ni_2P (denoted as xNP/CdS, x (%) = the theoretical mass fractions of Ni_2P) were synthesized using a facile solvothermal method (details in Experimental Section and Figure S1, Supporting Information). Among these, the 12% Ni_2P composite (12NP/CdS) was selected as the representative sample for characterizations due to its optimal photocatalytic activity (as elaborated below). The mass fraction of Ni_2P in the 12NP/CdS composite was determined to be ≈10.9% through inductively coupled plasma optical emission spectrometry (ICP-OES), which is close to the theoretical value (Table S1, Supporting Information). The powder X-ray diffraction (XRD) measurements in **Figure 1A** suggested that introducing Ni_2P has no impact on the crystal phase of CdS (JCPDS No. 41–1049). In the 12NP/CdS pattern, a weak peak attributed to the (111) lattice plane of Ni_2P (JCPDS No. 03–0953) was observed, which progressively became more prominent with an increase in Ni_2P content (Figure S2, Supporting Information). Further, X-ray photoelectron spectroscopy (XPS) was employed to investigate the valence states of Ni_2P and CdS. The full XPS spectrum confirmed the presence of Cd, S, Ni, and P elements (Figure S3A, Supporting Information). The primary Cd^{2+} peaks in CdS nanorods shifted to higher binding energies in the 12NP/CdS composite (Figure 1B), suggesting an electronic interaction between Ni_2P and CdS.[20] A similar shift in binding energy was also detected for S 2p spectra (Figure 1C). The Ni 2p spectra in Figure 1D revealed the coexistence of $Ni^{\delta+}$ and Ni^{2+} in Ni_2P,[21] with these peaks showing a negative shift after incorporation with CdS, signifying an electron transfer from CdS to Ni_2P. In the P 2p spectra of Ni_2P (Figure S3B, Supporting Information), peaks ≈129.3 and 133.8 eV can be assigned to $P^{\delta-}$ in Ni_2P and P^{5+} in phosphide clusters (e.g., PO_4^{3-}). The binding energy of $P^{\delta-}$ in the 12NP/CdS sample was lower than that of Ni_2P, in agreement with the observation of Ni^{2+}. Scanning electron microscopy (SEM) images (Figure S4A–G, Supporting Information) uncovered that the nanorod shapes of CdS and NP/CdS composites were retained. As the Ni_2P content increased, the

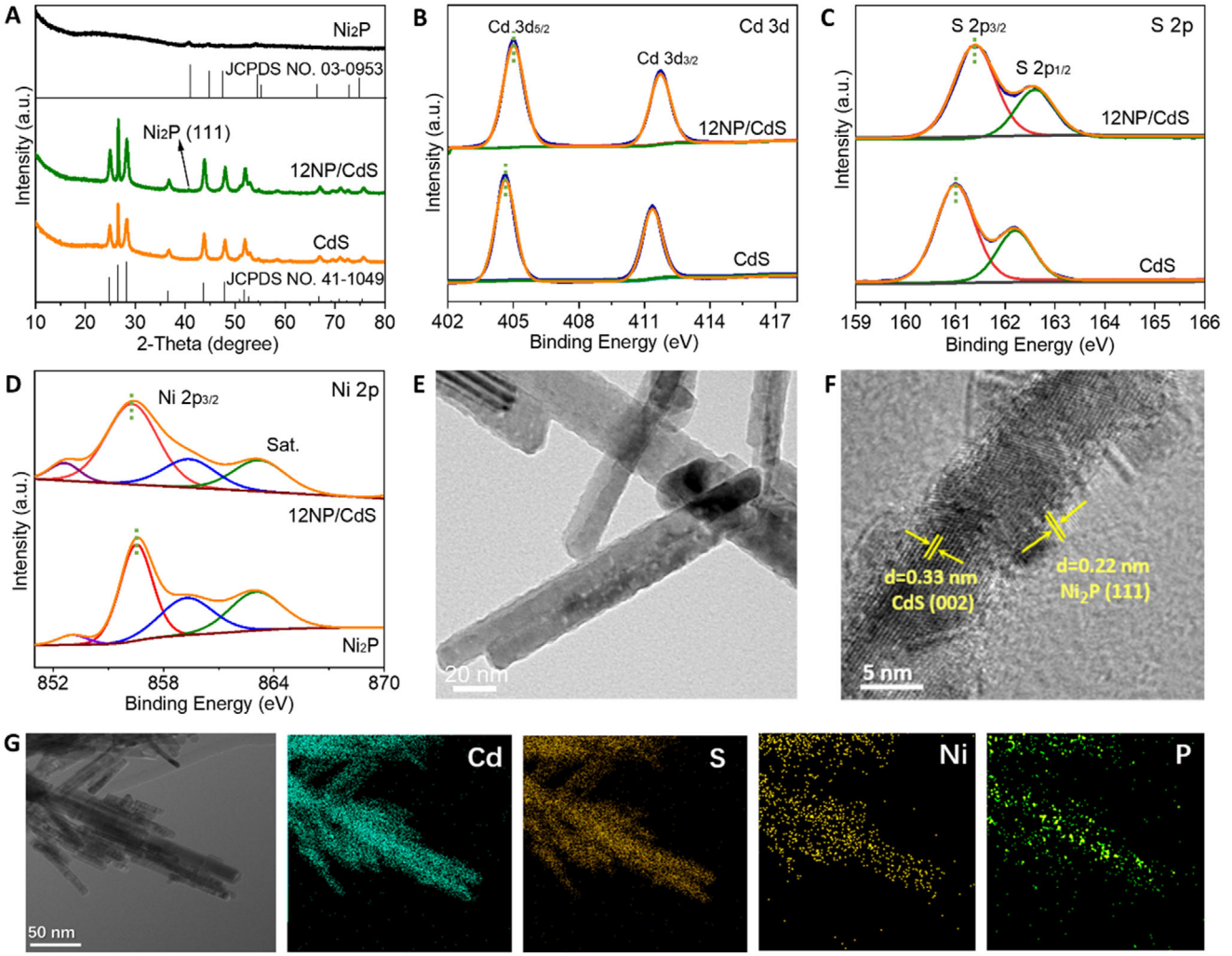

Figure 1. XRD patterns (A) of the prepared Ni_2P, CdS, and 12NP/CdS samples. XPS high-resolution spectra of Cd 3d (B), S 2p (C), Ni 2p (D) over CdS and 12NP/CdS samples. TEM (E) and HRTEM (F) images of 12NP/CdS composite; TEM image and the corresponding EDS-mapping images of Cd, S, Ni, and P elements (G).

Ni_2P nanosheets attached to the surfaces of CdS nanorods became more prominent. The transmission electron microscopy (TEM) and high-resolution TEM (HRTEM) images confirmed that the bare CdS and Ni_2P exhibited distinct nanorod-like and nanosheet-like morphologies, respectively, both with high crystallinity and pure crystal phases (Figures S5 and S6, Supporting Information). Notably, for the 12NP/CdS composite, its TEM image revealed that the CdS nanorods were wrapped by small, wrinkled Ni_2P nanosheets (Figure 1E). Furthermore, the HRTEM image of 12NP/CdS unveiled clear and distinctive lattice fringes with *d*-spacing values of 0.33 and 0.22 nm, indexed to the (002) facets of CdS and the (111) facets of Ni_2P, respectively (Figure 1F). This verified the successful formation of crystalline NP/CdS composite, in agreement with the XRD results. Besides, the TEM image and the corresponding energy-dispersive X-ray spectroscopy (EDS) mapping (Figure 1G) displayed an even distribution of Ni and P along the CdS nanorods, further supporting the coupling of Ni_2P and CdS.

2.2. Photoredox Catalysis Performances

The redox catalytic performance of the xNP/CdS composites was evaluated by examining the photocatalytic oxidation of BA into BAD and HB coupled with the reduction of CO_2 into syngas (CO and H_2) under visible light ($\lambda > 420$ nm) irradiation (**Figure** 2A). The product standard curve is shown in Figure S7 (Supporting Information). Control experiments in Table S2 (Supporting Information) confirmed the light-driven photocatalytic process, and isotope labeling experiments with $^{13}CO_2$ as reactants demonstrate that the produced ^{13}CO originates from $^{13}CO_2$ reduction (Figure S8, Supporting Information). As shown in Figure 2B, the production rate and selectivity of HB catalyzed by the bare CdS were only ≈2.3 μmol g^{-1} h^{-1} and ≈3.6%, respectively. Upon introducing Ni_2P, although the oxidation products were still BAD and HB (no other C—C coupling products such as benzoin or deoxybenzoin), both the formation rate and selectivity of HB were significantly enhanced. In particular, 12NP/CdS

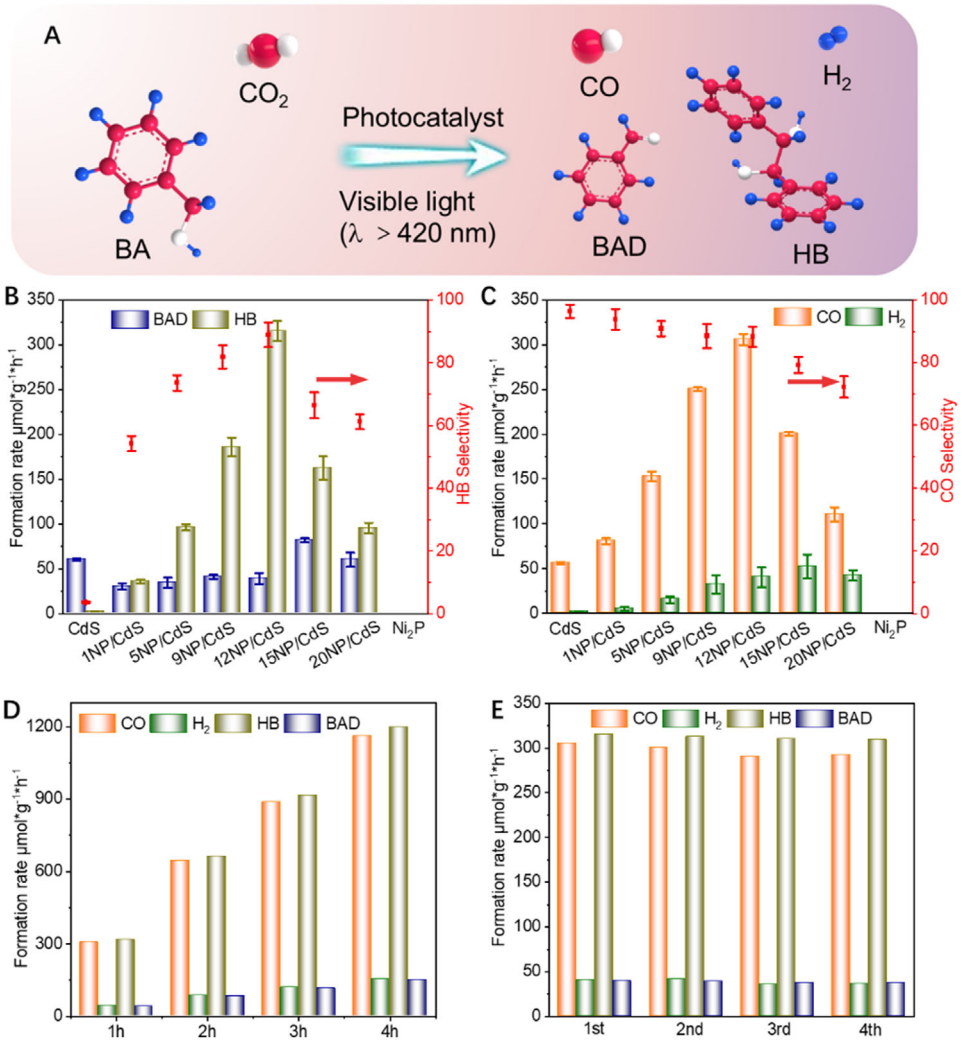

Figure 2. Schematic for the photoredox catalysis, which consisted of the oxidation of BA into BAD and HB coupled with the reduction of CO_2 into CO and H_2, under visible light ($\lambda > 420$ nm) irradiation (A). Photocatalytic BAD and HB (B) and CO and H_2 (C) production by bare CdS and different xNP/CdS samples. Extended irradiation time experiments (D) and recycled experiments of the representative 12NP/CdS (E).

achieved optimal performance with an impressive HB yield of ≈315.4 μmol g^{-1} h^{-1} and a selectivity of ≈90%. On the other hand, the formation rates of CO and H_2 by bare CdS were ≈56.4 and ≈2.1 μmol g^{-1} h^{-1}, respectively, with a CO/H_2 ratio of ≈27:1 (Figure 2C). Intriguingly, after introducing even 1% Ni_2P, the ratio of CO/H_2 from CO_2 reduction catalyzed by the as-obtained 1NP/CdS decreased to ≈15:1. The H_2 selectivity was further boosted with the increment of the Ni_2P content within the NP/CdS composites. Meanwhile, the CO/H_2 ratio exhibited a decreasing trend. Notably, 20NP/CdS can produce syngas with a CO/H_2 ratio of ≈2.6:1, which was particularly suitable for the industrial application of syngas fermentation.[22] Notably, the yield of the reduction products was maximized by 12NP/CdS, achieving formation rates of CO and H_2 at ≈305.7 and ≈40.2 μmol g^{-1} h^{-1}, respectively. This level of photoredox catalytic activity for concurrent BA oxidation and CO_2 reduction outperformed most state-of-the-art catalysts reported to date (Table S3, Supporting Information). Besides, no above-mentioned oxidation and reduction products (BAD, HB, CO, and H_2) from photoredox were detected in the case of the bare Ni_2P (Figure 2B,C), confirming its role as a mediator and that CdS was the active catalytic phase. To evaluate its universality in enhancing the photoredox catalysis, especially the HB production, we also synthesized Ni_2P-modified $ZnIn_2S_4$ (12%NP/ZIS4), $Cd_{0.6}Zn_{0.4}S$ (12%NP/CZS), and ZnO (12%NP/ZnO) composites (Figure S9A–C, Supporting Information), and subsequently examined their photocatalytic performances under the identical reaction conditions as those of NP/CdS. As shown in Figure S9D (Supporting Information), the incorporation of Ni_2P into all the semiconductor systems significantly improved both overall photocatalytic productivity and the selectivity of HB. To further verify the importance of chemically coupling Ni_2P in boosting photoredox catalysis, we conducted comparative experiments by physically mixing Ni_2P and CdS via stirring and grinding, both of which exhibited similar catalytic performances to those of the bare CdS (Figure S10, Supporting Information). These findings

directly and clearly evidenced the crucial effects of Ni_2P on promoting photocatalytic BA oxidation integrated with CO_2 reduction, with a particular role in improving HB formation. It is worth noting that the extended experiments involving photocatalytic CO_2 reduction and oxidation of different aromatic alcohols demonstrate the generally excellent capabilities (especially regarding the efficient and selective C—C chemicals generation) of 12NP/CdS, highlighting the broad applicability and practicality of the Ni_2P coupling strategy on the optimization of adsorption sites (Table S4, Supporting Information). In addition, time-dependent analysis in Figure 2D revealed a linear increment of products with extended irradiation time, and four successive recycling tests in Figure 2E demonstrated the photocatalytic stability of the NP/CdS composite. Most importantly, the post-reaction analysis confirmed that the crystal phase, crystallinity, and morphology of 12NP/CdS were retained well after four consecutive photoredox catalysis cycles (see XRD, TEM, and HRTEM data in Figure S11A–C, Supporting Information).

2.3. Origins of Enhanced Photoredox Catalytic Activity and Selectivity for NP/CdS

We conducted comprehensive ex situ/in situ characterizations combined with theoretical simulations to elucidate the factors contributing to the enhanced photoredox catalytic activity and selectivity for BA oxidation and CO_2 reduction upon the introduction of Ni_2P. UV–vis diffuse reflectance spectroscopy (UV–vis DRS) results in Figure S12 (Supporting Information) illustrate that coupling CdS with Ni_2P led to increased absorption in the long-wavelength region compared to the bare CdS. This enhancement can be attributed to the light absorption ability of black-colored Ni_2P (Figure S13, Supporting Information). The corresponding band gaps (E_g) of CdS and 12NP/CdS were determined to be 2.41 and 2.39 eV, respectively, based on Tauc plots (Figure S14, Supporting Information). Furthermore, the conduction band (CB) positions of the CdS and 12NP/CdS were evaluated using Mott–Schottky (M-S) plots. As illustrated in Figure S15A,B (Supporting Information), the flat band potentials (V_{fb}) of CdS and 12NP/CdS were found to be −0.35 and −0.29 V (vs. NHE), respectively. Since for n-type semiconductors, the CB potential is typically 0.1 V more negative than V_{fb},[16] the CB positions of CdS and 12NP/CdS were estimated to be −0.45 and −0.39 V (vs. NHE), respectively. These measurements indicate that the band structure of CdS remains largely unchanged after coupling with Ni_2P (Figure S16, Supporting Information). UV photoelectron spectroscopy (UPS) in Figure S17 (Supporting Information) disclosed different work functions for CdS (5.22 eV) and Ni_2P (6.36 eV), resulting in charge redistribution and band bending (Figure S18, Supporting Information), thereby forming an energy barrier at their interface.[23] Charge density difference was calculated via DFT calculation to gain deeper insights into the interfacial coupling between CdS and Ni_2P. The averaged charge redistributions in the (x-y) plane plotted as a function of distance along the z-direction are presented in **Figure 3A**, in which the red and green regions represent charge accumulation and depletion, respectively. These results reflected the significant charge redistribution, with electrons accumulating near the Ni_2P region and holes near the CdS region. This transfer of electrons from CdS to Ni_2P corroborates the results of XPS and UPS studies. The average electrostatic potential of the CdS-Ni_2P heterojunction (Figure 3B) displayed a potential drop of 13.0 eV, suggesting an appreciable built-in electronic field at the interface of NP/CdS composite directed from CdS to Ni_2P (Figure S18, Supporting Information).[24] Furthermore, the in situ XPS results (Figure S19, Supporting Information) show that upon light irradiation, the binding energies of Ni and P both negatively shifted, indicating that Ni_2P effectively accepted the photogenerated electrons from CdS, leading to electron accumulation over the Ni_2P with an enhanced reduction ability during the photoredox process.

Various photoelectrochemical and photoluminescence analyses were conducted to investigate the charge transfer behaviors in CdS and 12NP/CdS samples.[25–27] The transient photocurrent responses (Figure S20, Supporting Information), linear sweep voltammetry (Figure S21, Supporting Information), electrochemical impedance spectroscopy (Figure S22, Supporting Information), and photoluminescence (Figure S23, Supporting Information) findings collectively corroborated the facilitated transfer of photoexcited carriers and the reduced recombination of electron–hole pairs.[28] This enhancement can be attributed to the metallic property of Ni_2P with a strong electron conduction ability conducive to charge transport and separation.[20,29–31] Consequently, the presented photocatalytic activity of the 12NP/CdS composite was substantially elevated. The charge transport efficiency (η_{trans}) of CdS and 12NP/CdS was subsequently calculated by the ratio of photocurrent with or without adding methyl viologen dichloride ($MVCl_2$) as electron scavengers.[24] As depicted in Figure S24 (Supporting Information), 12NP/CdS exhibited a higher η_{trans} (94.9%) than that of CdS (75.9%), demonstrating the improved charge separation and transfer enabled by Ni_2P coupling.

The interfacial charge transfer kinetics of these samples were further probed by open-circuit voltage decay (OCVD) and the corresponding electron lifetime analysis.[32] As shown in Figure 3C, the 12NP/CdS sample showed a smaller decay rate compared to pure CdS after turning off the light irradiation, indicating reduced recombination of charge carriers. Moreover, based on OCVD results, the average photoelectron lifetime (τ) of 12NP/CdS was longer than that of CdS (Figure 3D). To understand the utilization rates of photoinduced holes (h^+) and electrons (e^-) during the reaction, in situ electron paramagnetic resonance (EPR) measurements were employed in the presence of (2,2,6,6-tetramethylpiperidin-1-yl)oxyl (TEMPO).[11,33,34] As depicted in Figure 3E,F, the EPR signal intensity of TEMPO decreased more significantly for 12NP/CdS upon the addition of BA compared to CdS. This result reveals that the introduction of Ni_2P leads to more efficient charge transfer and higher utilization of charge carriers during photoredox catalysis. Consequently, the photocatalytic performance was significantly enhanced.

To further investigate how the Ni_2P-modified CdS achieves efficient and selective conversion of BA to HB, as well as the precise adjustment of the CO/H_2 ratio for the production of industrially relevant syngas, we conducted a series of photochemical control experiments, ex situ/in situ characterizations, and theoretical calculations. First of all, the oxidative coupling of aromatic alcohols to produce the C—C coupling product HB was examined. Generally, the C—C coupling reaction is initiated

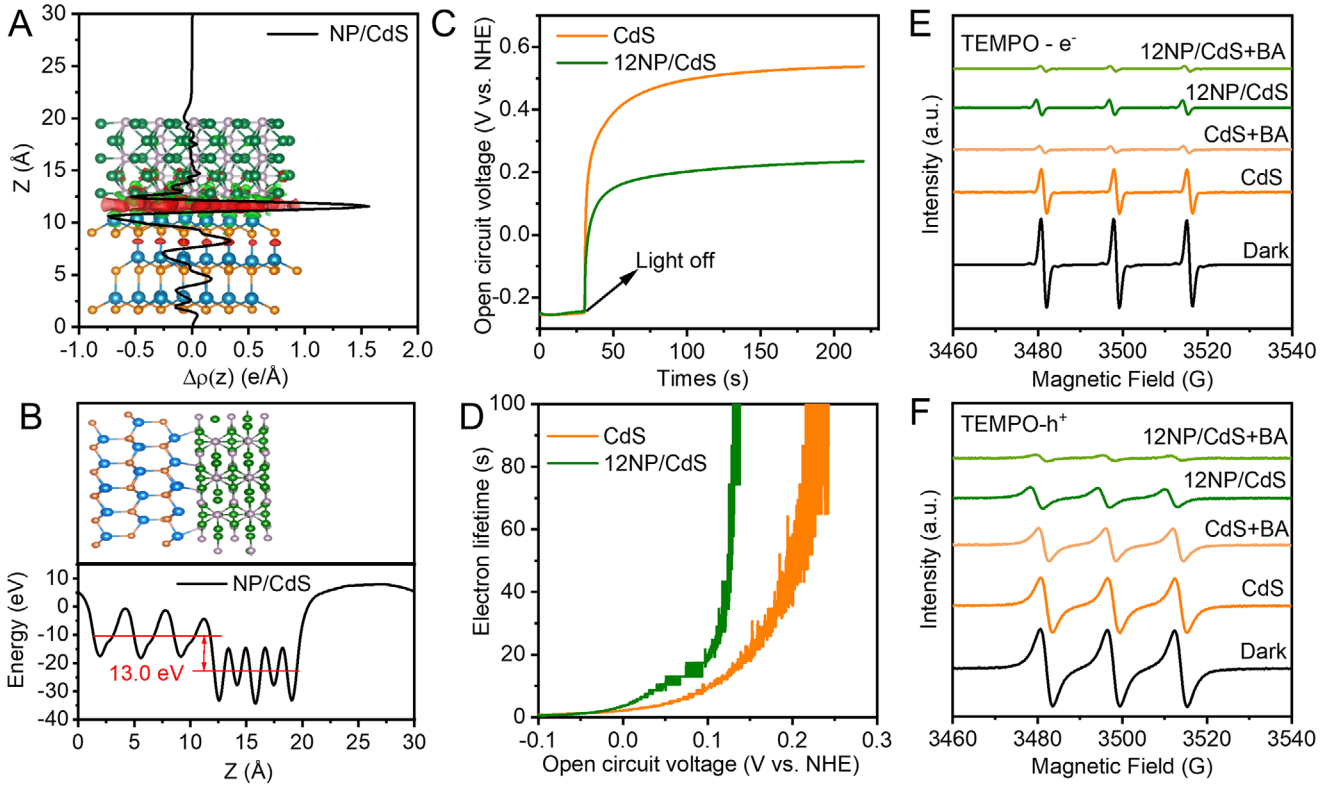

Figure 3. The profile of the planar averaged charge density difference for the CdS (001)-Ni_2P (001) heterojunction as a function of position along the z direction (A). The red and green isosurfaces indicate the accumulation and depletion of electrons, respectively. The calculated average electrostatic potential of CdS (001)-Ni_2P (001) heterojunction (B). Decay profiles of OCVD (C) and electron lifetimes (D) of the CdS and 12NP/CdS samples. In situ EPR spectra of TEMPO-e^- (E) and TEMPO-h^+ (F) for different catalysts under visible light irradiation ("Dark" meant the reaction system in the darkness). Note that the green, lavender, blue, and orange spheres in Figure 3A,B represent Ni, P, Cd, and S, respectively.

by carbon radicals (•CH(OH)Ph),[12,13] which were detected through in situ EPR spectra for both 12 NP/CdS and CdS (Figure S25, Supporting Information). More importantly, a stronger signal can be observed in the 12NP/CdS case, indicating that the introduction of Ni_2P promoted the formation of •CH(OH)Ph. Moreover, the DFT calculation was performed to investigate the adsorption ability of intermediates and products for NP/CdS and CdS. Specifically, regarding the NP/CdS composite, HB can be more easily desorbed compared to BAD (which could remain adsorbed at the interface between CdS and Ni_2P). In contrast, in the case of the bare CdS, the HB product tended to be adsorbed at the active sites, while BAD was desorbed from the surface more easily (**Figure** 4A,B). Due to its high concentration of negatively charged P, Ni_2P, a transition metal phosphide, is excellent at attracting protons within the system.[35,36] Benefiting from this aspect, the adsorbed BAD on the NP/CdS surface is likely to transform into carbon radicals, promoting the photocatalytic activity of C—C coupling to produce HB products. To further validate this conclusion, we introduced additional protons into the catalyst system by adding different amounts of hydrochloric acid (HCl) (Figure 4C), resulting in an apparently increased HB production. This is because the introduction of extra protons facilitated the generation of carbon radicals, as confirmed by in situ EPR characterization (Figure S26, Supporting Information). To further demonstrate that the enhanced HB generation is proton-induced rather than a result of water in the hydrochloric acid, we conducted control experiments by adding pure water and concentrated sulfuric acid. The experimental results shown in Figure S27A (Supporting Information) indicated that pure water failed to enhance the photocatalytic activity. Notably, the addition of concentrated sulfuric acid can pronouncedly enhance the yield of HB (Figure S27B, Supporting Information), further evidencing the pivotal role of accumulating protons in boosting the formation of carbon radical intermediates and, thus, the final HB products. In addition, these •CH(OH)Ph radicals may undergo further oxidation by holes to generate BAD or couple with other radicals to yield HB.[9] As explained earlier, to enhance the selectivity of HB production, facilitating the desorption of •CH(OH)Ph and HB from the catalyst surface in time is of great importance. In this respect, our DFT calculation results expounded that the CdS coupled with Ni_2P exhibited weaker adsorption strength toward •CH(OH)Ph intermediate compared with the pristine CdS (Figure 4A,B), which is believed to effectively prevent the consecutive oxidation of •CH(OH)Ph into BAD. Instead, the reaction route of coupling the neighboring •CH(OH)Ph to form HB is highly preferred.[8,9,12,13] Furthermore, the as-evolved HB can be readily desorbed from the catalyst surface, effectively inhibiting its further conversion into benzoin or deoxybenzoin.[9,13] Thus, incorporating Ni_2P into CdS enables the selective formation of a single C—C coupling product, HB.

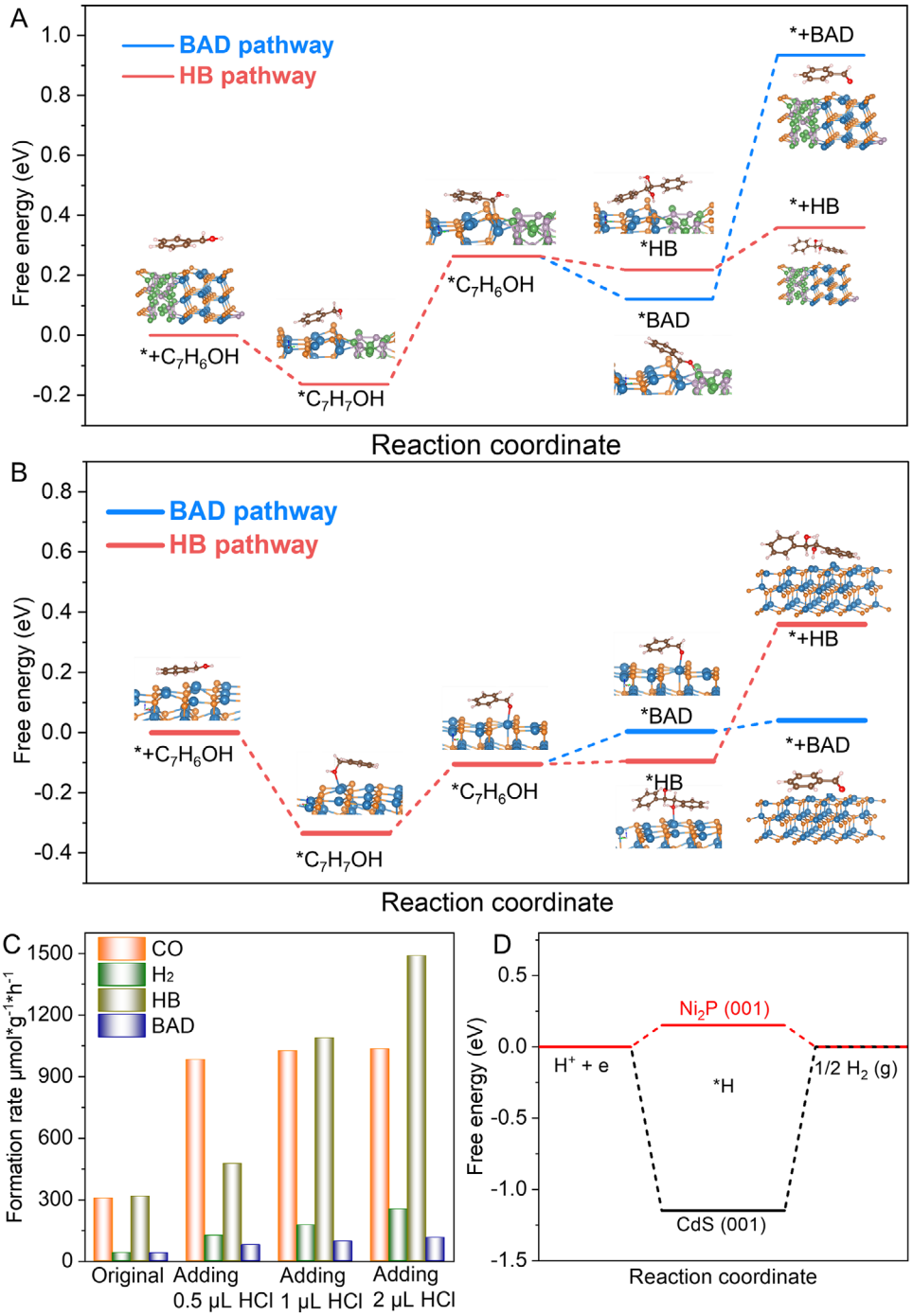

Figure 4. Free energy diagrams of BA oxidation to produce BAD and HB catalyzed by NP/CdS (A) and CdS (B). Photocatalytic oxidation of BA catalyzed by 12NP/CdS after adding different amounts of hydrochloric acid (C). Intermediate hydrogen adsorption free energy (ΔG_{H^*}) of CdS and Ni_2P (D). Note that the green, lavender, blue, orange, brown, red, and pink spheres in Figure 4A,B represent Ni, P, Cd, S, C, O, and H, respectively.

On the other hand, in situ diffuse reflection infrared Fourier transform (DRIFT) spectra were collected, which successfully detected different reaction intermediates of the photoredox cycle catalyzed by 12NP/CdS (details in Figure S28, Supporting Information). Notably, the first step for CO_2 reduction involves the adsorption and activation of CO_2 molecules on the catalyst surface,[4] which was also verified by in situ DRIFTS spectra. To gain further insights, DFT calculations on the adsorption of CO_2 by CdS and Ni_2P were performed (Figure S29, Supporting Information), which demonstrated that CdS can bind CO_2 readily, while Ni_2P is less favorable for CO_2 adsorption. This difference was further validated by the CO_2 adsorption isotherms of CdS and 12NP/CdS samples, where the introduction of Ni_2P reduced the adsorption capacity of CO_2 molecules (Figure S30,

Supporting Information). Notably, the Gibbs free energy calculation for the CO_2 reduction to CO demonstrates that the coupling of Ni_2P might thermodynamically improve the ability of CdS to catalyze the CO_2-to-CO (Figure S31, Supporting Information). However, when the Ni_2P incompetent at adsorbing CO_2 was over-incorporated, the productivity of CO deteriorated, as indicated by the photocatalytic formation rate of CO in Figure 2C. Additionally, for H_2 evolution, an ideal catalyst should have an intermediate hydrogen adsorption free energy (ΔG_{H^*}) with a value of zero, which means the optimum adsorption and desorption of such a critical intermediate, and consequently, enhanced performance for H_2 generation.[34,37,38] As shown in Figure 4D, the ΔG_{H^*} of Ni_2P was much closer to zero compared with that of CdS, illustrating that Ni_2P was more favorable for intermediate hydrogen adsorption and desorption. This explains why the Ni_2P phase was more active for H_2 production than the CdS phase. Therefore, increasing the content of Ni_2P within the NP/CdS system elevated the selectivity of H_2 among the photocatalytic reduction products (Figure 2C). Besides, the hydrogen temperature-programmed desorption (H_2-TPD) experiments (Figure S32, Supporting Information) of 12NP/CdS showed a wider desorption temperature range than that of CdS, implying the presence of different kinds of adsorption sites induced by the incorporation of Ni_2P.[39] Moreover, 12NP/CdS displayed a desorption peak at a relatively lower temperature range compared to CdS, highlighting its enhanced hydrogen adsorption ability.[40] These results confirm that the introduction of Ni_2P can distinctly improve the H_2 generation ability. Based on the above analysis, the ratio of CO and H_2 as reduction products in photocatalysis can be controllably tuned by adjusting the content of catalyst phases with varying CO_2 affinity and H_2 production abilities. As a result, the industrially applicable syngas with a controlled CO/ H_2 can be attained.

3. Conclusion

In summary, a novel NP/CdS composite was synthesized for photoredox catalysis, integrating BA oxidation and CO_2 reduction. Notably, NP/CdS with optimum Ni_2P content efficiently catalyzed the C—C coupling of BA, achieving a HB yield of ≈315.4 μmol g^{-1} h^{-1} and a selectivity of ≈90%. Concurrently, the ratio of CO and H_2 can be precisely tuned over a wide range (from ≈15:1 to ≈2.6:1) by increasing the content of Ni_2P within this composite. The exceptional photoredox catalytic activity and selectivity can be attributed to the introduction of Ni_2P, which enabled the active sites with stronger adsorption of BADs and protons. This facilitated the formation of the critical •CH(OH)Ph intermediate and C—C coupling HB, thus elevating the catalytic activity. Further, such intermediates and products were efficiently desorbed from the catalyst surface, ensuring the high selectivity of HB production. At the same time, by modifying the content of the Ni_2P phase, which had a poor affinity for CO_2 but a better capability for H_2 production, the active sites within CdS/Ni_2P responsible for CO and H_2 evolution were optimized. Based on this, the CO/H_2 ratio was finely tuned, enabling the production of industrially applicable syngas. Our work offers a new approach for the robust and selective production of particular C—C coupling chemicals and syngas with specific CO/H_2 ratios, based on a direct and facile photoredox cycle.

Supporting Information

Supporting Information is available from the Wiley Online Library or from the author.

Acknowledgements

J.L. and H.Y. contributed equally to this work. This work was supported by the National Natural Science Foundation of China (NSFC, 52002142), the Foundation of Anhui Province for Distinguished Young Scholars (2022AH020038). A portion of this work was performed on the Steady High Magnetic Field Facilities, High Magnetic Field Laboratory, CAS. P.W.M. greatly acknowledges support from the German Federal Ministry of Education and Research in the project Catlab (03EW0015A/B) framework.

Conflict of Interest

The authors declare no conflict of interest.

Data Availability Statement

The data that support the findings of this study are available from the corresponding author upon reasonable request.

Keywords

adsorption site manipulation, benzyl alcohol oxidation, carbon dioxide reduction, hydrobenzoin, photoredox catalysis, tunable syngas

Received: February 17, 2025
Revised: April 6, 2025
Published online: May 2, 2025

[1] Z. Gao, J. Mu, J. Zhang, Z. Huang, X. Lin, N. Luo, F. Wang, *J. Am. Chem. Soc.* **2022**, *144*, 18986.
[2] R. Wang, L. Shi, E. Y. Konysheva, X. Xu, *Adv. Funct. Mater.* **2024**, *34*, 2418074.
[3] G. Han, X. Liu, Z. Cao, Y. Sun, *ACS Catal.* **2020**, *10*, 9346.
[4] Q. Guo, F. Liang, X. Li, Y. Gao, M. Huang, Y. Wang, S. Xia, X. Gao, Q. Gan, Z. Lin, C. Tung, L. Wu, *Chem* **2019**, *5*, 2605.
[5] J. Tang, J. He, S.-Y. Zhao, W. Liu, *Angew. Chem., Int. Ed.* **2023**, *17*, 202215882.
[6] S. M. A. H. Siddiki, N. T. Toyao, K. Shimizu, *Green Chem.* **2018**, *20*, 2933.
[7] S. P. Morcillo, D. Miguel, A. G. Campaña, L. Á. Cienfuegos, J. Justicia, J. M. Cuerva, *Org. Chem. Front.* **2014**, *1*, 15.
[8] Z. Huang, P. Sun, H. Zhang, H. Zhang, S. Zhang, Z. Chen, X. Yi, S. Xie, *ACS Catal.* **2024**, *14*, 4581.
[9] S. G. Lee, M. J. Kang, M. Park, K. Kim, H. Lee, H. S. Kim, *Appl. Catal. B* **2022**, *304*, 120967.
[10] S. Xie, Z. Shen, J. Deng, P. Guo, Q. Zhang, H. Zhang, C. Ma, Z. Jiang, J. Cheng, D. Deng, Y. Wang, *Nat. Commun.* **2018**, *9*, 1181.
[11] J. Lei, H. Yang, Z. Chen, S. Meng, N. Zhou, Y. Yang, P. W. Menezes, *Adv. Energy Sustainability Res.* **2023**, *4*, 2300122.
[12] J. Wang, M. Qi, X. Wang, W. Su, *Appl. Catal. B* **2022**, *302*, 120812.
[13] M. Qi, Q. Lin, Z. Tang, Y. Xu, *Appl. Catal. B* **2022**, *307*, 121158.
[14] Q. Liu, J. Lin, H. Cheng, L. Wei, F. Wang, *Angew. Chem., Int. Ed.* **2023**, *62*, 202218720.
[15] B. Weng, M. Zhang, Y. Z. Lin, J. C. Yang, J. Q. Lv, N. Han, J. F. Xie, H. P. Jia, B.-L. Su, M. Roeffaers, J. Hofkens, Y. F. Zhu, S. B. Wang, W. Y. Choi, Y.-M. Zheng, *Nat. Rev. Clean Technol.* **2025**, *1*, 201.

[16] J. Wang, E. Kim, D. P. Kumar, A. P. Rangappa, Y. Kim, Y. Zhang, T. K. Kim, *Angew. Chem., Int. Ed.* **2022**, *61*, 202113044.
[17] J. Lei, N. Zhou, S. Sang, S. Meng, J. Low, Y. Li, *Chin. J. Catal.* **2024**, *65*, 163.
[18] K. Lu, J. Hao, Y. Wei, B. Weng, S. Ge, K. Yang, S. Lu, M. Yang, Y. Liao, *Inorg. Chem.* **2024**, *63*, 795.
[19] M. Lin, W. Jiang, T. Zhang, B. Yang, Z. Zhuang, Y. Yu, *Small Sci.* **2023**, *3*, 2200085.
[20] Z. Wang, Z. Qi, X. Fan, D. Y. C. Leung, J. Long, Z. Zhang, T. Miao, S. Meng, S. Chen, X. Fu, *Appl. Catal. B* **2021**, *281*, 119443.
[21] Q. Wang, Z. Zhang, C. Cai, M. Wang, Z. Zhao, M. Li, X. Huang, S. Han, H. Zhou, Z. Feng, L. Li, J. Li, H. Xu, J. Francisco, M. Gu, *J. Am. Chem. Soc.* **2021**, *143*, 13605.
[22] Z. Liang, L. Song, M. Sun, B. Huang, Y. Du, *Sci. Adv.* **2021**, *7*, abl4915.
[23] P. Zhang, C. Xue, Y. Li, S. Guo, X. Zhang, P. Zhang, G. Shao, *Chem. Eng. J.* **2021**, *404*, 126497.
[24] J. Wan, L. Liu, Y. Wu, J. Song, J. Liu, R. Song, J. Low, X. Chen, J. Wang, F. Fu, Y. Xiong, *Adv. Funct. Mater.* **2022**, *32*, 2203252.
[25] F. Arcudi, L. Đorđević, N. Schweitzer, S. Stupp, E. Weiss, *Nat. Chem.* **2022**, *14*, 1007.
[26] X. Wu, Q. Li, S. Zuo, Y. Li, X. Yi, L. Yuan, L. Zheng, J. Zhang, J. Dong, S. Wang, H. Zhang, J. Zhang, *Nano Lett.* **2023**, *23*, 11562.
[27] Y. Tian, R. Wang, S. Deng, Y. Tao, W. Dai, Q. Zheng, C. Huang, C. Xie, Q. Zeng, J. Lin, H. Chen, *Nano Lett.* **2023**, *23*, 10914.
[28] G. Jia, Z. Wang, M. Gong, Y. Wang, L. H. Li, Y. Dong, L. Liu, L. Zhang, J. Zhao, W. Zheng, X. Cui, *Carbon Energy* **2023**, *5*, 270.
[29] C. Tang, R. Zhang, W. Lu, Z. Wang, D. Liu, S. Hao, G. Du, A. M. Asiri, X. Sun, *Angew. Chem, Int. Ed.* **2017**, *56*, 842.
[30] S. Meng, C. Chen, X. Gu, H. Wu, Q. Meng, J. Zhang, S. Chen, X. Fu, D. Liu, W. Lei, *Appl. Catal. B* **2021**, *285*, 119789.
[31] A. Indra, A. Acharjya, P. W. Menezes, C. Merschjann, D. Hollmann, M. Schwarze, M. Aktas, A. Friedrich, S. Lochbrunner, A. Thomas, M. Driess, *Angew. Chem., Int. Ed.* **2017**, *56*, 1653.
[32] S. Li, Q. Mo, S. Zhu, Z. Wei, B. Tang, B. Liu, H. Liang, Y. Xiao, G. Wu, X. Ge, F. Xiao, *Adv. Funct. Mater.* **2022**, *32*, 2110848.
[33] J. Zhang, Y. Hu, H. Li, L. Cao, Z. Jiang, Z. Chai, X. Wang, *Inorg. Chem.* **2021**, *60*, 15782.
[34] H. Zhang, Y. Gao, S. Meng, Z. Wang, P. Wang, Z. Wang, C. Qiu, S. Chen, B. Weng, Y.-M. Zheng, *Adv. Sci.* **2024**, *11*, 2400099.
[35] H. Yang, P. Guo, R. Wang, Z. Chen, H. Xu, H. Pan, D. Sun, F. Fang, R. Wu, *Adv. Mater.* **2022**, *34*, 2107548.
[36] P. W. Menezes, A. Indra, C. Das, C. Walter, C. Göbel, V. Gutkin, D. Schmeißer, M. Driess, *ACS Catal.* **2017**, *7*, 103.
[37] Z. Chen, R. Wu, Y. Liu, Y. Ha, Y. Guo, D. Sun, M. Liu, F. Fang, *Adv. Mater.* **2018**, *30*, 1802011.
[38] Z. Chen, S. Mebs, I. Mondal, H. Yang, H. Dau, Z. Kang, M. Haumann, S. Ghosh, W. Cen, M. Driess, P. W. Menezes, *Adv. Funct. Mater.* **2024**, 2402699.
[39] H. Huang, K. Liu, F. Yang, J. Cai, S. Wang, W. Chen, Q. Wang, L. Fu, Z. Xie, S. Xie, *Angew. Chem., Int. Ed.* **2023**, *62*, 202315752.
[40] Y. Liang, J. He, Y. An, J. Zhang, G. Park, L. Zhao, R. Oh, X. Huang, J. Dong, L. Liu, *Chem. Eng. J.* **2024**, *484*, 149670.